Letter

Solar Thermoplasmonic Nanofurnace for High-Temperature Heterogeneous Catalysis

Alberto Naldoni,* Zhaxylyk A. Kudyshev, Luca Mascaretti, Smritakshi P. Sarmah, Sourav Rej,
Jens P. Froning, Ondřej Tomanec, Jeong Eun Yoo, Di Wang, Štěpán Kment, Tiziano Montini,
Paolo Fornasiero, Vladimir M. Shalaev, Patrik Schmuki, Alexandra Boltasseva,* and Radek Zbořil*

Cite This: https://dx.doi.org/10.1021/acs.nanolett.0c00594

Read Online

ACCESS | Metrics & More | Article Recommendations | SI Supporting Information

ABSTRACT: Most of existing solar thermal technologies require highly concentrated solar power to operate in the temperature range 300−600 °C. Here, thin films of refractory plasmonic TiN cylindrical nanocavities manufactured via flexible and scalable process are presented. The fabricated TiN films show polarization-insensitive 95% broadband absorption in the visible and near-infrared spectral ranges and act as plasmonic "nanofurnaces" capable of reaching temperatures above 600 °C under moderately concentrated solar irradiation (∼20 Suns). The demonstrated structures can be used to control nanometer-scale chemistry with zeptoliter (10^{-21} L) volumetric precision, catalyzing C—C bond formation and melting inorganic deposits. Also shown is the possibility to perform solar thermal CO oxidation at rates of 16 mol h^{-1} m^{-2} and with a solar-to-heat thermoplasmonic efficiency of 63%. Access to scalable, cost-effective refractory plasmonic nanofurnaces opens the way to the development of modular solar thermal devices for sustainable catalytic processes.

KEYWORDS: plasmonics, titanium nitride, solar-thermal, solar chemicals, nanocavity, sustainable catalysis
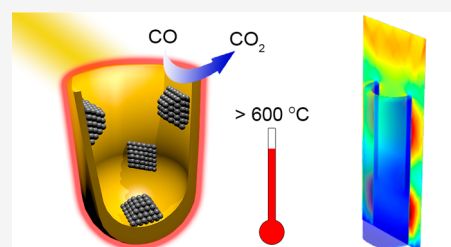
The efficient generation and management of heat is a key challenge for the global energy sector. Heating and cooling account for 52% of society's overall energy consumption, 10% of which is produced from renewables. Solar thermal technologies account for only 7% of the world's renewable heat generation, highlighting the extreme need for novel and efficient solar-to-heat energy conversion technologies.[1]

Present solar thermal technologies such as parabolic troughs and solar towers operate in the temperature range 300−600 °C and generate renewable electricity. Such high temperatures can only be reached by achieving concentrated solar powers of the order of 100−1000 Suns, which are attainable by implanting large area solar plants (i.e., 50 ha for a 50 MW implant) that in turn require extremely high capital costs (i.e., US $400 million).[2]

Solar thermal technologies hold promise not only for generating renewable electricity but also for the development of chemical implants that use the high-generated temperatures to catalyze sustainable chemical transformations such carbon dioxide reduction, hydrogen generation, and liquid fuels synthesis through the Fischer−Tropsch process.

However, high-temperature catalysis may only become market-competitive through the development of compact, cost-effective thin-film devices that need lower concentrated solar power (and thus cheaper optical components) to reach high operating temperatures.

Plasmonics, or metal nano-optics, offers unprecedented control over light at the nanoscale and has stimulated both new fundamental research and novel application concepts in applied optics,[3] photochemistry,[4,5] and nanoelectronics.[6,7] The illumination of metal nanostructures excites surface plasmons whose dissipation causes local temperature rise. Thermoplasmonics is a subfield of plasmonics in which these losses are exploited as nanoscale sources of heat.[8,9] Since the early 2000s, the light-induced heating of metal nanoparticles has found applications in photothermal cancer therapy.[10,11] Local heating has also been used in applications such as catalysis,[12] steam generation,[13] and desalination.[14] Unfortunately, the applicability of nanoparticle-based systems is limited by their low stability at high temperatures which causes the nanoparticles to aggregate over time.

There have recently been significant advances in the development of thermoplasmonic thin film systems, which overcome the intrinsic limitations of nanoparticles and have found applications in areas such as templated growth of nanostructures,[15,16] optical nanotweezers,[17−20] heat-assisted
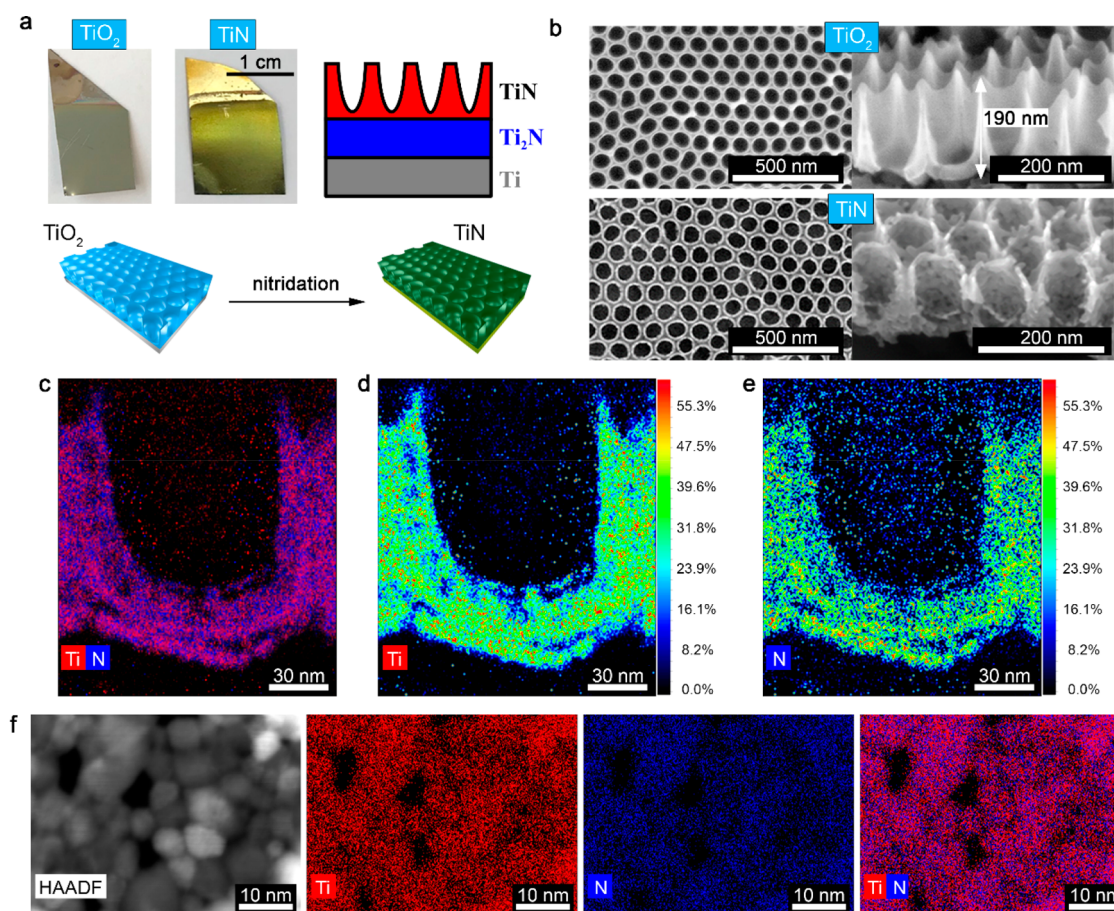
Figure 1. Structure and composition of TiN nanofurnaces. (a) Photographic image and schematic representation of TiO_2 nanocavities and TiN nanofurnaces. (b) SEM images showing top and cross-sectional views of TiO_2 nanocavities and TiN nanofurnaces. (c) HRTEM micrographs obtained by EDS elemental mapping for Ti (red) and N (blue) of a lamella prepared by focused ion beam micromachining. (d,e) Deconvoluted elemental mapping for Ti and N showing their atomic concentrations in the same lamella. (f) HAADF scanning TEM image and EDS elemental mapping for Ti (red) and N (blue) of crystallites forming the bottom of a single TiN nanofurnace.

magnetic recording,[21−23] and energetic materials.[24] However, the thermoplasmonic devices reported to date use micrometer-sized patterns and focused laser excitation to achieve the desired conditions and temperatures and are therefore unsuitable for practical applications requiring large-scale solar-to-heat energy conversion.

Photonic crystals are an interesting exception because they are easily fabricated on large areas without compromising their optical properties. This was recently exploited to design efficient absorbers/emitters for (solar) thermophotovol-taics.[25−27]

Here, we introduce a scalable, flexible method of fabricating solar absorbers utilizing refractory plasmonic titanium nitride (TiN) nanostructures with periodicity and unit cell dimensions being an order of magnitude smaller than those typical of photonic crystals. The resulting two-dimensional (2D) subwavelength cylindrical nanocavity arrays can be fabricated over square-centimeter areas and perform as broadband absorbers capable of concentrating the dissipated optical power in zeptoliter volumes, thus generating temperatures exceeding 600 °C under moderately concentrated solar radiation. Each nanocavity acts as a "nanofurnace" (or nanoreactor), enabling thermally induced nanochemistry with unprecedented reported volumetric precision and inducing the melting and decomposition of an iron organometallic precursor and new C—C bond formation, ultimately leading

to the deposition of a conformal layer of crystalline hematite. We also show that metal nanoparticle-decorated TiN nanofurnaces catalyze CO oxidation, a model reaction, at a solar-to-heat thermoplasmonic efficiency of 63%.

■ RESULTS AND DISCUSSION

Fabrication of Plasmonic Nanofurnaces. The studied thermoplasmonic nanofurnaces are made using TiN, an emerging refractory plasmonic material with high thermo-stability.[28−31]

TiN exhibits metallic properties in the visible and near-infrared ranges and CMOS compatibility, making it an attractive alternative plasmonic material to traditional noble metals.[30−33] Plasmonic TiN nanoantennas have been success-fully used in second-harmonic generation,[30] heat-assisted magnetic recording,[23] water evaporation,[29] plasmon-enhanced photoelectrochemical water splitting,[34] and as broadband absorbers for solar thermophotovoltaics.[35] Notably, recent investigations revealed that at temperatures above 400 °C the figures of merit of localized surface plasmon resonances (LSPRs) and propagating surface plasmon polaritons (SPPs) in thin TiN films are almost identical to those of polycrystalline noble metals.[31,36−38] These optical properties, together with its exceptional mechanical hardness, thermal and structural stability, and chemical inertness, make plasmonic TiN an
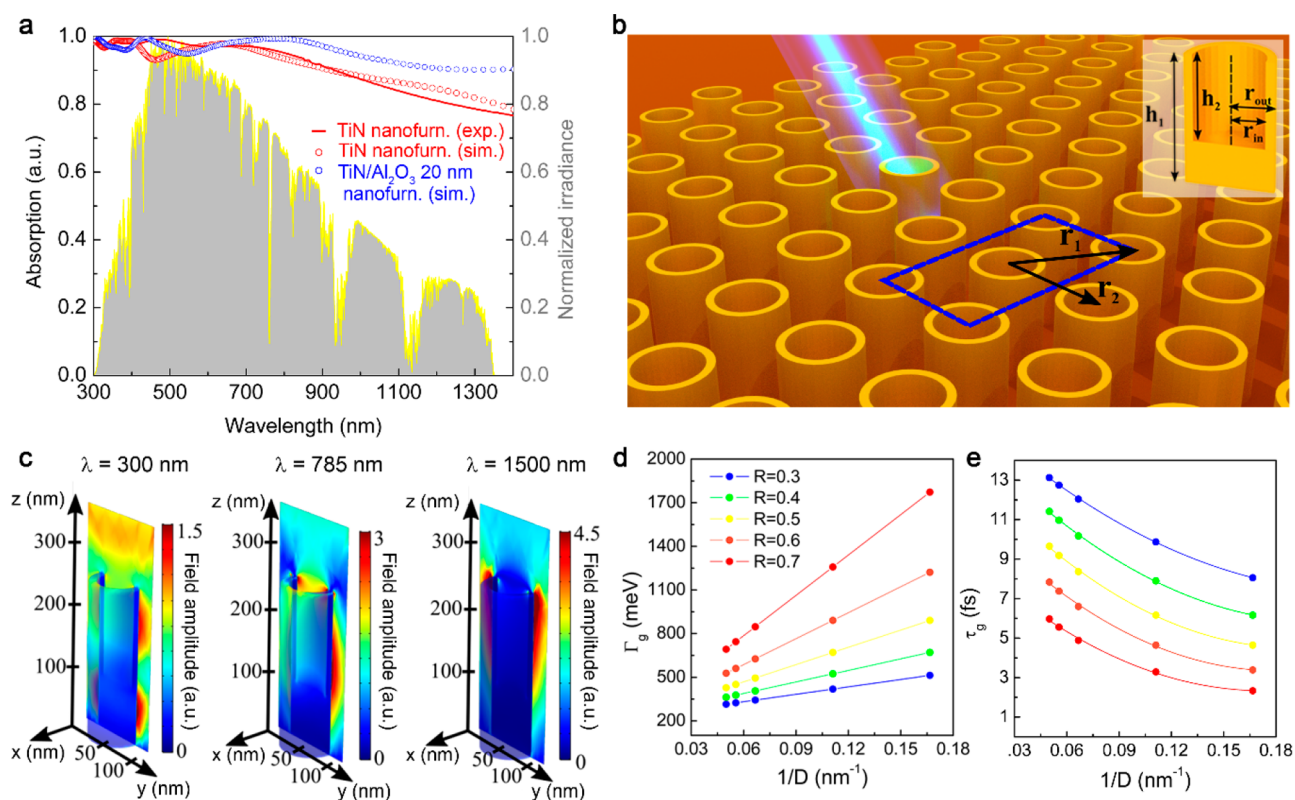
Figure 2. Optical properties of TiN nanofurnaces. (a) Absorption spectra of TiN nanofurnaces (experimental, red line; simulated for normal incidence, hollow red circles), TiN nanofurnaces covered with a 20 nm Al_2O_3 layer (simulated for normal incidence, hollow blue circles), and normalized irradiance of the AM 1.5G solar spectrum (gray shaded area). (b) Schematic depiction of a TiN nanofurnace array on a $Ti_2N–Ti$ substrate. Each nanofurnace is a closed cylindrical structure with inner and outer radii of r_{in} = 30 nm and r_{out} = 45 nm, respectively. The total height of a single nanofurnace is h_1 = 250 nm; the inner height is h_2 = 165 nm. The substrate is a multilayered structure comprising a 1 μm thick Ti_2N layer on a Ti substrate. (c) Simulated absolute electric field amplitude distributions for three excitation wavelengths (λ_1 = 300 nm, λ_2 = 785 nm, λ_3 = 1500 nm) showing the effects of exciting different optical modes. (d,e) Dependence of the electron relaxation rate (Γ_g; d) and electron relaxation time (τ_g; e) on the inverse grain size (1/D), calculated using the Mayadas model[41,42] with different values of the electron reflection coefficient (R).

ideal candidate material for efficient and robust solar thermal devices.

In this work, TiN nanofurnaces were fabricated using a two-step approach involving the anodization of a Ti foil to form TiO_2 nanocavities with subsequent nitridation under an ammonia atmosphere (Figure 1a). The anodization process produces highly homogeneous TiO_2 nanocavity arrays that self-organize into close-packed hexagonal lattices (Figure 1b and Figure S1). Anodization is widely utilized to prevent corrosion and is therefore an economical and easily scalable approach that can be used to produce nanostructures over large areas.[39] Additionally, TiO_2 is a ubiquitous material in optoelectronics with multiple well-developed fabrication routes. Therefore, TiO_2 nitridation is a convenient strategy for preparing subwavelength plasmonic TiN nanostructures that avoids the need for costly fabrication steps.[40]

Upon nitridation, the nanostructured TiO_2 films turn from pale blue to dark green or violet, depending on the nanofurnace length (generally in the range 150−200 nm), suggesting the formation of plasmonic TiN (see Figure 1a,b). After ammonia treatment, the TiO_2 nanocavities are fully nitridized to form TiN nanofurnaces with an average diameter of 80 nm, length of 180 nm, wall thickness of about 20 nm, and center-to-center distance of 100 nm (Figure 1b,c). The nanofurnaces thus have internal volumes of ∼750 zeptoliters ($10^{−21}$ L). The crystal cell volume contracts by 42% during the conversion of TiO_2 to TiN, which imposes significant

mechanical stress on the nanostructures that are released by the transformation of the close-packed TiO_2 nanocavities into cylindrical TiN nanofurnaces with slightly separated walls.

Figure 1c−e shows high resolution transmission electron microscopy (HRTEM) images obtained by energy-dispersive X-ray spectroscopy (EDS) elemental mapping of a lamella of our TiN thin film. These images of a single TiN nanofurnace show that nitridation establishes a degree of porosity on both the bottom and the walls of the nanofurnaces, which may influence the optical losses of our plasmonic device. Moreover, a superposition of the titanium and nitrogen mappings reveals that both elements are evenly distributed at atomic resolution (Figure 1c), while deconvoluted elemental maps (Figure 1d,e) indicate that TiN nanofurnaces contain equal molar quantities of Ti and N; the material's content of each element is close to 50%, as expected for stoichiometric TiN.

Interestingly, micrographs of the bottom of a single TiN nanofurnace showed its walls to be polycrystalline, consisting of very small crystallites with an average size of 9 nm (Figure 1f).

Further morphological analysis showed that the gradient diffusion of ammonia through the solid surfaces of our samples during nitridation caused the formation of multilayer films with an upper layer of pure cylindrical TiN nanofurnaces above a Ti_2N layer with a thickness of ∼1 μm sitting on a Ti substrate (for further characterizations, see also Figures S2−S8).
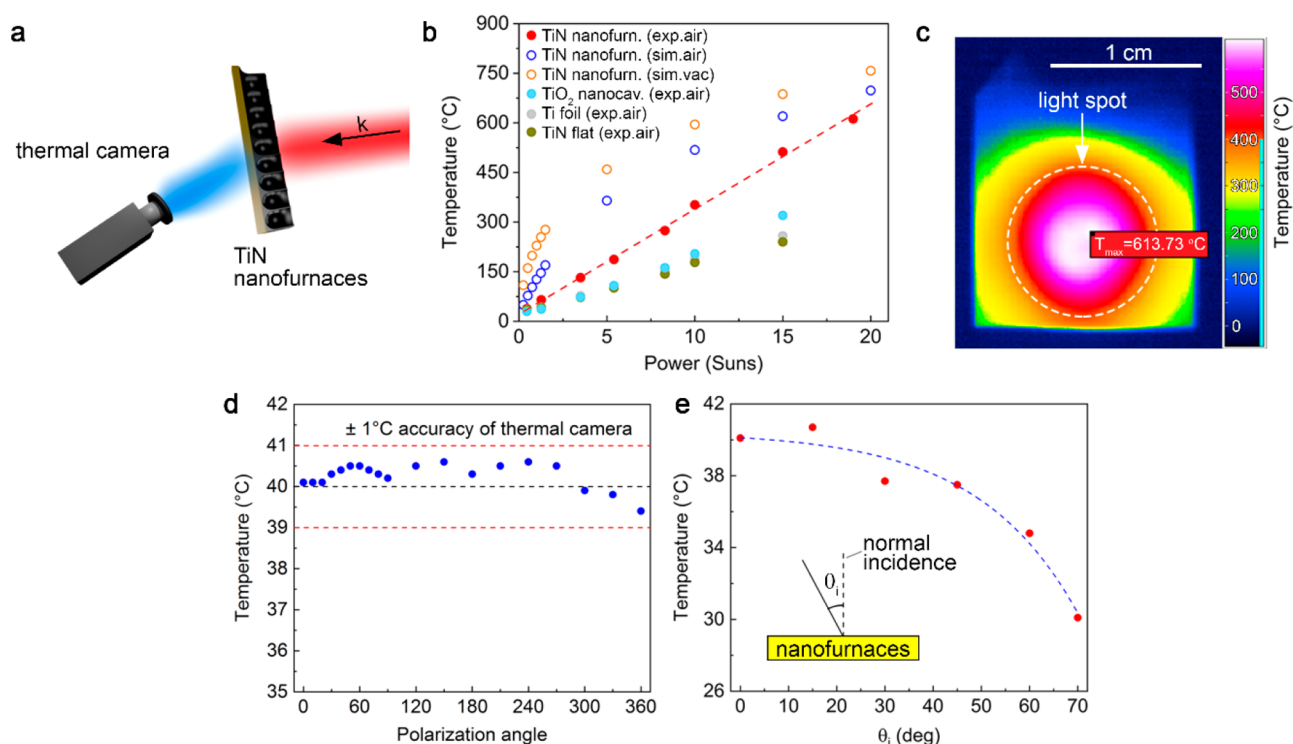
Figure 3. Light-to-heat energy conversion with TiN nanofurnaces. (a) Schematic depiction of the experimental setup for thermal measurements. (b) Experimental (filled circles) and simulated (hollow circles) dependence of the generated temperature on the solar power expressed in Suns (1 Sun = 100 mW cm^{-2}). (c) Experimental infrared camera image showing the thermal gradient around the illuminated central spot for TiN nanofurnaces under 19 Suns. (d) Measured dependence of the temperature on the polarization angle of an incident 785 nm laser excitation with a spot radius of 2.5 mm. (e) Dependence of the temperature on the angle (θ_i) of incidence for 785 nm laser excitation with a spot radius of 2.5 mm and a power of 105 mW.

Optical Properties of Plasmonic Nanofurnaces. A key feature to achieve efficient nanoscale heat generation is the engineering of the optical response of plasmonic nanofurnaces.

Nanofurnaces sit on an optically thick 125 μm Ti foil that hinders light transmission. Optical absorption was therefore estimated measuring reflection (R) at normal incidence and using the expression for the absorption as $A = 1 - R$ (provided transmission T is 0). The demonstrated TiN nanofurnaces are broadband absorbers that capture the solar spectrum (Figure 2a, gray shaded area) with near-unity efficiency: their average absorption over the visible range (380−700 nm) is 98%, peaking at 99% at 470 nm (Figure 2a, red solid line). The average absorptivity decreases slightly (to 95%) over the wider wavelength range of 300−1100 nm and falls to 77% if the upper wavelength limit is extended to 1400 nm. Absorptivity above 90% could be maintained even at these wider wavelength ranges by depositing a 20 nm layer of a dielectric material such as Al$_2$O$_3$ (Figure 2a, hollow blue circles) on the TiN nanofurnaces. This raised their average absorption between 300 and 2000 nm to 96% and may also protect against TiN oxidation.

To better understand the optical properties of the nanofurnace array, we performed full-wave electromagnetic simulations using the complex dielectric permittivity of TiN from temperature-dependent ellipsometry measurements.[38] The dimensions of nanofurnaces and the unit cell were chosen to give the best possible agreement with the experimental absorption spectra while remaining within the experimentally verified parameter space (Figure 2b and Methods in the Supporting Information).

The simulated absorption spectrum of TiN nanofurnaces (Figure 2a, red hollow dots) agrees well with the experimental trace over a wide range of wavelengths (Figure 2a, red solid line).

Figure 2c shows electric field (E-field) distributions for three excitation wavelengths: $\lambda_1 = 300$ nm (pure cavity resonance), $\lambda_2 = 785$ nm (hybrid resonance), and $\lambda_3 = 1500$ nm (off-resonance).

The system's resonant behavior is determined by the fundamental waveguide mode of the cylindrical TiN nanofurnaces,[43] which is characterized by the corresponding cutoff wavelength ($\lambda_c = 1130$ nm) (see also Figures S9 and S10). Radiation with wavelengths below λ_c is effectively coupled into cavity modes and its absorption is enhanced by prolonged interaction times and TiN optical losses. Some of the excited modes are standard cavity modes, while others are hybrid cavity and SPP modes (hybrid resonance).[26,43]

Excitation of the pure cavity modes produces efficient light−matter interaction, resulting in the highest absorption in the visible range (99% at 470 nm). The nanofurnace array's high density of cavity modes and the optical losses of TiN instead lead to broadband absorption across the visible and near-IR ranges, centered at 785 nm with a full-width-half-maximum of 700 nm. The exceptional broadening of this resonance could also be due to the roughness and presence of voids in the TiN nanofurnaces (see Figure 1c−e). The electric field (E-field) distribution at 785 nm (Figure 2c, λ_2) shows the excitation of both the first order cavity mode and the SPP waves propagating along the vertical sidewalls of the nanofurnaces.

Finally, absorption under off-resonance conditions (λ_3 = 1500 nm) is due to the LSPR on the corners of the nanofurnaces.

A strategy for manipulating the light-to-heat conversion efficiency is to tune the electron relaxation rate (Γ), which is a fundamental parameter of surface plasmons that quantifies the overall quality[44] of the resonances.

Our TiN nanofurnaces form polycrystalline films whose grain size (6−20 nm) is much lower than the mean free path of electrons in TiN (i.e., ∼45 nm)[45] and can be tuned by varying the processing temperature (see Figure S6). Within this grain size regime, the grain boundary scattering contribution to the optical properties becomes significant, and both relaxation times (τ_g) and relaxation rates ($\Gamma_g = \tau_g^{-1}$) can be estimated using the model of Mayadas[41] through the simple expression

$$\tau_g^{-1} = \tau_0^{-1} + \frac{1.37\nu_F R}{D(1 - R)} \tag{1}$$

where $\tau_0^{-1} = \Gamma_0$ is the relaxation rate for infinite grain size, which was determined to be 230 meV[38] for single crystalline TiN films at room temperature, $\nu_F = 7 \times 10^5$ m s^{-1} is the Fermi velocity for TiN,[45] D is the average grain diameter, and R is the electron reflection coefficient at grain boundaries. The grain boundary reflection coefficient, R, is often taken to be 0.5 as a first approximation, but values between 0.3 and 0.7 have been reported.[44,46−49]

Figure 2d presents the values of Γ_g for TiN nanofurnaces with different grain sizes and shows that grain scattering strongly affects Γ_g in our films. For D = 6 nm, Γ_g is almost 2-fold (513 meV, R = 0.3), 4-fold (819 meV, R = 0.5), or 8-fold (1772 meV, R = 0.7) the reference value for TiN single crystals, depending on the choice of R. The values obtained for TiN nanofurnaces are very high, especially when compared with the Γ_g of gold nanostructures, which was reported to be between 30 and 90 meV for crystal sizes of 40−200 nm.[44,46−48] As expected, we also obtained very short electron relaxation times for TiN nanofurnaces (Figure 2e). For example, the value of τ_g of 4.6 fs (R = 0.5) for D = 6 nm is 3-fold lower than typical values reported for Au and Ag.[47,48]

These results suggest that TiN nanofurnaces have high optical losses and that the generation of heat by the dissipation of their electrons' momentum can be controlled by tuning grain size.

Solar-to-Heat Energy Conversion in Thermoplasmonic Nanofurnaces. To assess the TiN nanofurnaces' thermoplasmonic performance, samples were excited at normal incidence (unless indicated otherwise) and an infrared (IR) camera was placed on the back of the films at a 30° angle (Figure 3a and Figure S11) to detect temperature variations. Each measurement was performed in air after the system reached a steady-state temperature and was corrected based on the experimental emissivity values (see Methods section and Table S1).

Figure 3b shows that the solar-induced heat generation in TiN nanofurnaces greatly outperforms that in TiO$_2$ nanocavities, Ti foil, and flat TiN reference samples.

When the TiN nanofurnace film was illuminated with a solar power of 19 Suns, we observed a solar thermoplasmonic temperature generation of 613 °C (for further measurements see also Figures S12−S14). The TiN nanofurnaces' outstanding performance is emphasized by the fact that similar temperatures have previously been reached only by using a laser with a 10^6-fold greater power density.[24] Despite the high thermal conductivity of the Ti substrate employed here, high

temperatures above 600 °C were generated, leaving much room for heat management improvement by thermally isolating the TiN nanofurnaces with substrates that can sustain high temperatures and with low thermal conductivity such as quartz, glass wool, and fiber/foam glass.

TiN nanofurnaces exhibit a power-dependent heating of 32.55 °C Suns^{-1} and take between 20 and 30 s to reach steady-state temperature generation (Table S2). They thus tolerate a heating/cooling rate of ∼25 °C s^{-1}, indicating exceptional resistance to thermal stress.

Interestingly, the maximum temperatures reached in the nanofurnaces depend linearly on the TiN grain size (Figure S15), confirming the intimate relationship between electron scattering at grain boundaries, dissipation of electron momentum, and thermoplasmonic heat generation.

To confirm the TiN nanofurnaces' remarkable thermoplasmonic heating performance, we performed finite-element heat transport simulations of nanofurnaces exposed to different excitation wavelengths from the solar spectrum (see Methods in the Supporting Information). The dissipated power was determined for each wavelength (Q_i), and the total dissipated power (Q_{tot}) was determined by integrating Q_i over the broadband solar spectrum. The total dissipated power was then treated as a heat source when solving the quasi-static heat transfer problem.

The total dissipated power inside a TiN nanofurnace (Figure S16) decreased in the order Q_1 (λ_1 = 300 nm) > Q_2 (λ_2 = 785 nm) > Q_3 (λ_3 = 1500 nm), as expected from the E-field intensity distribution maps (Figure 2c). Irradiation at λ_1 = 300 nm, exciting the pure cavity mode, causes power to be dissipated all along the nanofurnace walls, but significant losses are also generated inside the nanofurnace base. A similar situation arose for the cavity−SPP hybrid resonances (λ_2 = 785 nm), although in this case there was very little dissipation in the base of the nanofurnace. Conversely, excitation at 1500 nm (the LSPR mode) produced only marginal power dissipation at the edges of the nanofurnace.

One of the key properties of the proposed nanofurnace structure is an efficient light to heat conversion rate. This is ensured not only by the proper optical response of the structure (broadband absorption) but also by the large mode overlap of the cavity modes with the highly lossy plasmonic material. Specifically, the mode analysis of the cavity modes shows that most of the energy is absorbed inside the thick plasmonic walls of the TiN nanofurnace. This leads to the high local heat generation rates, which is essential for photocatalytic reactions. Some photonic crystal structures can ensure similar broadband absorption. However, due to the not optimal spatial cavity mode distribution and/or the low optical losses of the host material platforms such photonic crystal structures do not ensure efficient local heat generation as in the case of TiN nanofurnaces.

The temperatures generated in air under solar illumination (Figure 3b, hollow blue circles) in the simulations differed slightly from the experimental values (red dots). However, at higher solar powers, the difference between the experimental and simulated values was only ∼50−70 °C. This slight discrepancy may be due to the mismatch between the TiN nanofurnace film size (2 cm × 1.5 cm) and the diameter of the focused light beam (∼1 cm) used in the experiments (these values coincide instead in the simulation). In addition, we used a Fresnel lens to focus solar light; lenses of this type generally create a strong gradient in light focus that results in a gradient
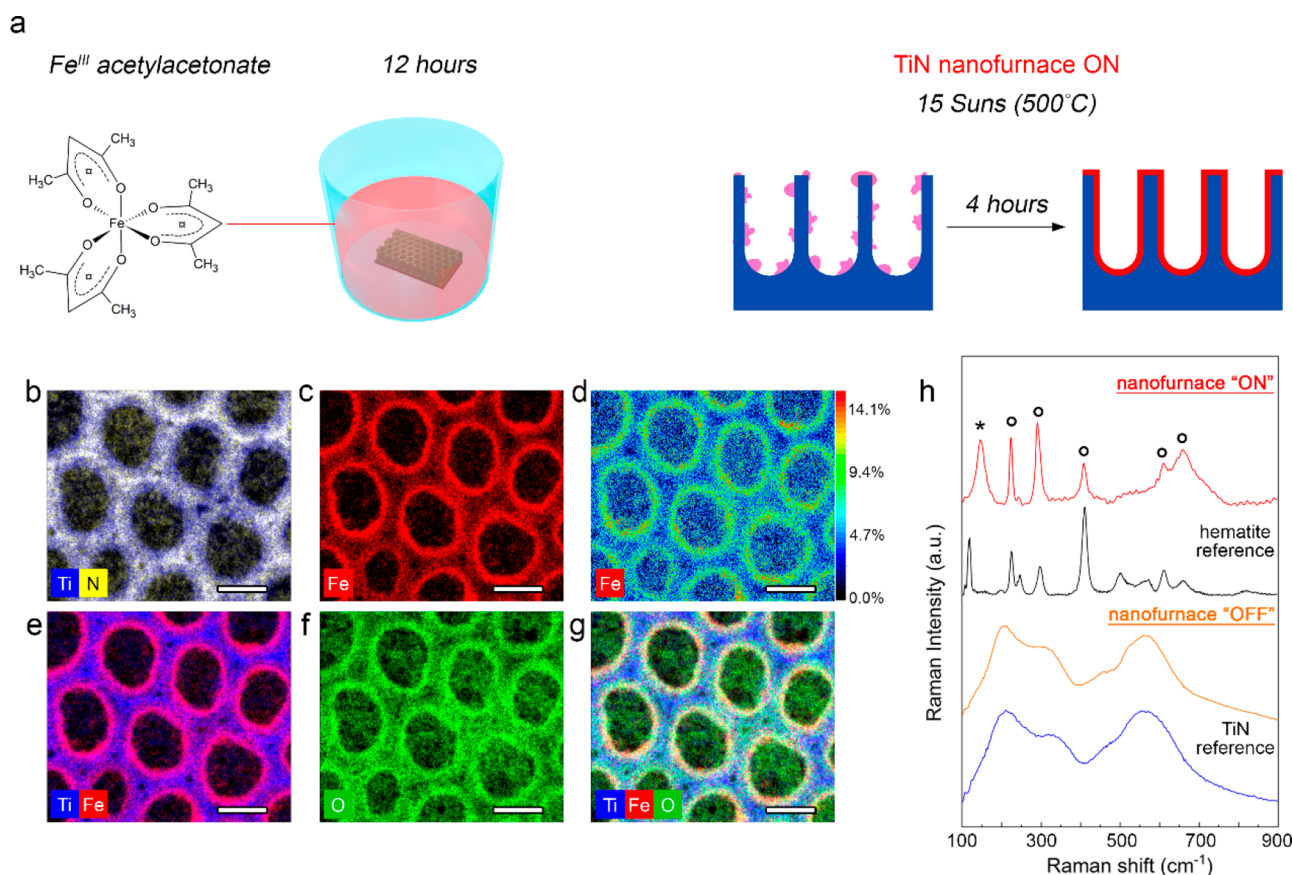
Figure 4. Nanofurnace demonstration. (a) Schematic representation of the procedure used in the nanofurnace demonstration experiments. (b,c,e–g) EDS elemental maps of TiN nanofurnaces after immersion in Fe^{III} acetylacetonate solution and irradiation with 15 Suns for 4 h in vacuum. (d) Deconvoluted EDS map showing the elemental distribution of Fe in coated nanofurnaces quantitatively. (h) Raman spectra of pristine TiN nanofurnaces (blue line), TiN nanofurnaces immersed in $Fe(acac)_3$ before irradiation (orange line), a reference hematite spectrum (black line), and a TiN nanofurnace after immersion in $Fe(acac)_3$ and irradiation with 15 Suns for 4 h in vacuum (red line). Hollow black circles indicate hematite bands, and the asterisk indicates the band assigned to anatase TiO_2.

of generated temperatures, as shown in the IR thermal image presented in Figure 3c, while in simulation we are assuming uniform concentration of the solar power within a spot.

Two additional factors that strongly affect the performance of solar energy conversion devices are (i) the polarization, and (ii) the angle of incidence of the incident light. The impact of these factors was investigated using a 785 nm laser with a power of 105 mW.

Polarization-dependent excitation generated a temperature of 40 ± 1 °C at all linear polarization angles (Figure 3d), in agreement with the absorption data (Figure S10). Thus, because of their cylindrical symmetry, the nanofurnaces behave as ideal polarization-insensitive solar thermal devices.

Additionally, heat generation in the thermoplasmonic TiN nanofurnaces show a constant response for a broad range of excitation angles ($\theta_i \in [-40°, 40°]$), while the optical response significantly deviates under large angle illumination (Figure 3e).

We next investigated the operational efficiency of TiN nanofurnaces at 15 Suns irradiation. First, we computed the thermal losses associated with convection (P_{conv}), which are given by

$$P_{conv} = hA(T - T_0) \tag{2}$$

where $h = 10$ W m^{-2} K^{-1} is the heat transfer coefficient (see Methods in the Supporting Information), $A = 1$ cm^2 is the

surface area of the nanofurnaces, T is the thermoplasmonic temperature generated in the nanofurnaces, and T_0 is room temperature.

Second, radiative losses (P_{rad}) were computed by integrating the blackbody radiation spectrum at the temperature generated inside the nanofurnaces, accounting for the spectral emissivity function and are given by

$$P_{rad} = A \int_{\lambda_{min}}^{\infty} \varepsilon(\lambda) I_{BB}(\lambda, T) d\lambda \tag{3}$$

where $\varepsilon(\lambda)$ is the emissivity of the nanofurnace surface and I_{BB} is the blackbody irradiance at the operating temperature, which is given by

$$I_{BB}(\lambda, T) = \frac{2\pi h c^2}{\lambda^5} \frac{1}{\exp\left(\frac{hc}{\lambda k_B T}\right) - 1} \tag{4}$$

where $h = 6.626 \times 10^{-34}$ J s^{-1} and $k_B = 1.381 \times 10^{-23}$ J K^{-1} are the Planck and Boltzmann constants, respectively, and $c = 2.998 \times 10^8$ m s^{-1} is the speed of light.

Using Kirchhoff's law, which states that a surface's emissivity equals its absorption, we computed the nanofurnaces' absorption spectrum from the experimentally determined complex dielectric permittivity of TiN at high temperatures[38] and used these values to compute P_{rad}.
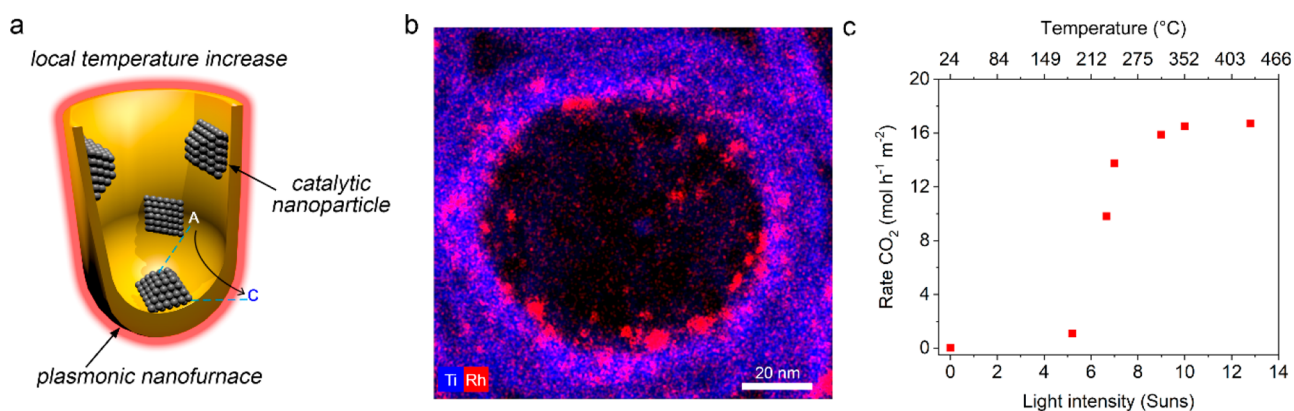
Figure 5. Solar-thermal catalysis. (a) Schematic representation of the concept of TiN nanofurnaces for solar-thermal catalysis. (b) EDS elemental map of a single TiN nanofurnace decorated with Rh nanoparticles. (c) Rate of CO_2 production from CO oxidation at different solar light intensities (AM 1.5G) and corresponding generated temperatures measured using the thermal camera.

Conduction losses were negligible because the samples were suspended using a metallic clamp placed at one of nanofurnaces edges, where the metal foil was close to room temperature.

Finally, we computed the thermoplasmonic solar-to-heat conversion efficiency (η_{STP}), which is given by

$$\eta_{STP} = \frac{P_{in} - P_{conv} - P_{rad}}{P_{in}} \times 100 \quad (5)$$

where P_{in} is the power of the incident light.

According to this model, when TiN nanofurnaces operate in air under 15 Suns irradiation and generate a temperature of 520 °C, the thermal losses are $P_{conv} = 0.495$ W and $P_{rad} = 0.480$ W. We thus obtain η_{STP} (air) = 35%; by excluding P_{conv} (which do not occur in vacuum), we obtain η_{STP} (vacuum) = 68%. An additional discussion on TiN nanofurnaces under different gas atmosphere may be found in the SI (Figures S17−S21).

Zeptoliter-Scale Chemistry with Thermoplasmonic Nanofurnaces. To demonstrate the practical potential of TiN nanofurnaces, we immersed the nanofurnaces in an acetone solution of $Fe^{III}(acac)_3$ (iron acetylacetonate) for 12 h, rinsed with acetone, and dried them under a nitrogen flow (Figure 4a). This induced the precipitation of submicrometric particles on top of the nanofurnaces and irregular deposits inside the nanofurnaces, without affecting the average diameter of each nanofurnace (see Figures S22−S27). When illuminated at 15 Suns in vacuum for 4 h (at η_{STP} = 68%), TiN nanofurnaces generated high temperatures in excess of 600 °C, causing the deposited Fe to melt and form a 10 nm thick conformal coating. This indicates that deposits formed at plasmonic hot spots of the TiN nanofurnaces, where heat dissipation is maximized. HAADF−STEM and EDS elemental mapping images demonstrated the atomic homogeneity of the deposited overlayer at subnanometer scales (Figure 4b−g). The micrographs also reveal that the nanofurnaces' walls were covered with a FeO_x layer and that the nanofurnaces retained their initial Ti and N atomic distributions.

To identify the FeO_x phase deposited onto the surface of TiN nanofurnace walls, we analyzed several areas of different samples before and after irradiation (Figure 4h). Raman spectroscopy revealed that only the fingerprint of TiN could be detected when the nanofurnace was in the OFF state (i.e., before irradiation). Conversely, after operation in the ON state (i.e., after irradiation at 15 Suns), sharp and well-defined peaks

typical of hematite (α-Fe_2O_3) appeared together with an additional peak associated with anatase TiO_2, which probably grew at the interface between TiN and α-Fe_2O_3 (see Figure 4b−g). The different relative intensity of α-Fe_2O_3 Raman peaks observed on the TiN film with respect to the reference α-Fe_2O_3 can be due to complex composition and substrate effect of the nanofurnaces.

Furthermore, the Raman spectra of nanofurnaces after thermocycling feature two very intense peaks due to the D and G bands of graphitic materials (Figure S28), demonstrating that the temperatures generated inside the nanofurnaces not only suffice to trigger the reaction of the organometallic Fe precursor but also lead to new C—C bond formation.

Solar-Thermal Heterogeneous Catalysis. To prove the concept of using TiN nanofurnaces for solar thermal catalysis, we use the model CO oxidation reaction promoted by different solar intensities. Figure 5a illustrates the concept of using TiN nanofurnaces decorated with catalytic nanoparticles for heterogeneous catalysis. To clearly show the power of this approach, we deposited Rh nanoparticles by immersing a nanofurnace film in ultrapure water containing $RhCl_3$ as a metal precursor, which was then reduced to Rh^0 by the addition of an aqueous solution of ammonia borane. As a result, we obtained Rh nanoparticles with size of 3−5 nm homogeneously distributed over the surface of the TiN nanofurnaces film (Figure S29). Figure 5b shows the EDS elemental map for Ti and Rh of a single TiN nanofurnace and highlights that the Rh nanoparticles were deposited both on the mouth and on the inner part of the thermoplasmonic cavity.

We tested the prepared TiN/Rh nanofurnaces in the CO oxidation to CO_2 by generating different temperatures at varying light intensities (Figure 5c). In dark conditions, we did not observe any formation of an appreciable amount of CO_2, while during solar irradiation the CO_2 formation rate increased rapidly and reached a plateau of ~16 mol h^{-1} m^{-2} of CO_2 at ~9 Suns irradiation and at a generated temperature of ~325 °C. At the same time, a stoichiometric O_2 conversion was observed. The conversion activity for CO oxidation was always in the range of 93−95%.

Notably, the light intensity dependence of the CO_2 generation rate follows the sigmoidal shape typical of thermally activated catalytic processes. The thermoplasmonic TiN nanofurnaces activated Rh nanoparticles that catalyzed the CO oxidation with naked TiN nanofurnaces that did not show

any significant activity, that is, 0.24 mol h^{-1} m^{-2} at 15 Suns irradiation generating a temperature above 500 °C. We finally computed the η_{STP} of the nanofurnaces during the CO oxidation, choosing the conditions at which the catalytic conversion rate reached 50% of the final value, that is, light intensity of 6.7 Suns and temperature of 235 °C. Following the approach presented in the previous section, when TiN nanofurnaces operate in air under 6.7 Suns irradiation and generate a temperature of 235 °C, the thermal losses are P_{conv} = 0.21 W and P_{rad} = 0.037 W. We thus obtain η_{STP} (air) = 63% and by excluding P_{conv} (which does not occur in vacuum), we obtain η_{STP} (vacuum) = 94.5%. Considering that the CO gas molecules may affect the convection losses similarly to air, our TiN/Rh nanofurnaces catalyzed CO oxidation at a solar-to-heat conversion efficiency of 63%.

In order to evaluate the nanofurnace stability, TiN nanofurnaces were tested in CO oxidation after a treatment with an accelerated aging protocol under 15 Suns irradiation and flowing CO and O$_2$ (Figure S30). The catalytic conversion rate reached 50% of the final value at a light intensity of 8.4 Suns and a temperature of 291 °C, thus showing a partial deactivation with respect to the pristine sample (Figure 5c) and likely associated with the beginning of TiN oxidation[50] as suggested by XPS analysis (Figure S31). Notably, if the TiN nanofurnaces were treated instead with an accelerated aging protocol under Ar, they showed very minor structural modifications (Figure S31), suggesting their higher stability for reactions performed in reducing conditions such as the challenging and environmentally relevant hydrogenation of carbon dioxide and ammonia synthesis.

CONCLUSION

We demonstrated scalable, cost-efficient solar thermoplasmonic thin films utilizing refractory plasmonic TiN by combining simple anodization and nitridation process that yielded centimeter-scale nanofurnaces. The demonstrated plasmonic nanostructures showed broadband solar absorption and produced temperatures exceeding 600 °C under moderately concentrated solar power, achieving a remarkable 68% solar-to-heat conversion efficiency. The unparalleled optical and thermal properties of the refractory TiN nanofurnaces enabled the concentration of a high optical power in zeptoliter-scale volumes and promoted the conformal deposition of iron oxide and formation of graphitic nanocarbons. We also showed that TiN nanofurnaces can host catalytic metal nanoparticles and can activate them for driving relevant heterogeneous catalytic reactions.

TiN nanofurnaces manufactured though the proposed scalable and cheap process have the potential to power thermally driven kW-scale solar thermal technologies, offering dramatic advantages over conventional approaches (i.e., solar towers) that typically require 1–2 orders of magnitude higher irradiation powers to reach similar operational temperatures.

The demonstrated nanofurnace design achieves exceptional efficiencies at temperatures up to ~600 °C. Above these temperatures, radiative losses increase rapidly, decreasing the system's efficiency. This efficiency drop could be mitigated by designing refractory plasmonic nanostructures with different unit cells and periodic arrangements, paving the way to the extreme temperature regime by enabling selective absorption and emission. This would open up additional practical applications in thermophotovoltaic and thermoelectric systems.

ASSOCIATED CONTENT

ⓢ Supporting Information

The Supporting Information is available free of charge at https://pubs.acs.org/doi/10.1021/acs.nanolett.0c00594.

Methods, additional structural and optical characterization, solar-to-heat measurements and simulations, stability tests, demonstration of nanofurnaces (PDF)

AUTHOR INFORMATION

Corresponding Authors

Alberto Naldoni − *Regional Centre of Advanced Technologies and Materials, Faculty of Science, Palacký University Olomouc, 78371 Olomouc, Czech Republic;* orcid.org/0000-0001-5932-2125; Email: alberto.naldoni@upol.cz

Alexandra Boltasseva − *School of Electrical and Computer Engineering and Birck Nanotechnology Center, Purdue University, West Lafayette, Indiana 47907, United States;* Email: aeb@purdue.edu

Radek Zbořil − *Regional Centre of Advanced Technologies and Materials, Faculty of Science, Palacký University Olomouc, 78371 Olomouc, Czech Republic;* orcid.org/0000-0002-3147-2196; Email: radek.zboril@upol.cz

Authors

Zhaxylyk A. Kudyshev − *School of Electrical and Computer Engineering and Birck Nanotechnology Center, Purdue University, West Lafayette, Indiana 47907, United States;* orcid.org/0000-0002-6955-0890

Luca Mascaretti − *Regional Centre of Advanced Technologies and Materials, Faculty of Science, Palacký University Olomouc, 78371 Olomouc, Czech Republic;* orcid.org/0000-0001-8997-7018

Smritakshi P. Sarmah − *Regional Centre of Advanced Technologies and Materials, Faculty of Science, Palacký University Olomouc, 78371 Olomouc, Czech Republic*

Sourav Rej − *Regional Centre of Advanced Technologies and Materials, Faculty of Science, Palacký University Olomouc, 78371 Olomouc, Czech Republic*

Jens P. Froning − *Regional Centre of Advanced Technologies and Materials, Faculty of Science, Palacký University Olomouc, 78371 Olomouc, Czech Republic*

Ondřej Tomanec − *Regional Centre of Advanced Technologies and Materials, Faculty of Science, Palacký University Olomouc, 78371 Olomouc, Czech Republic*

Jeong Eun Yoo − *Department of Materials Science and Engineering, University of Erlangen-Nuremberg, D-91058 Erlangen, Germany*

Di Wang − *School of Electrical and Computer Engineering and Birck Nanotechnology Center, Purdue University, West Lafayette, Indiana 47907, United States;* orcid.org/0000-0002-3536-7027

Štěpán Kment − *Regional Centre of Advanced Technologies and Materials, Faculty of Science, Palacký University Olomouc, 78371 Olomouc, Czech Republic*

Tiziano Montini − *Department of Chemical and Pharmaceutical Sciences, INSTM and ICCOM-CNR, University of Trieste, Trieste 34127, Italy*

Paolo Fornasiero − *Department of Chemical and Pharmaceutical Sciences, INSTM and ICCOM-CNR, University of Trieste, Trieste 34127, Italy;* orcid.org/0000-0003-1082-9157

Vladimir M. Shalaev − *School of Electrical and Computer Engineering and Birck Nanotechnology Center, Purdue University, West Lafayette, Indiana 47907, United States*

Patrik Schmuki − *Regional Centre of Advanced Technologies and Materials, Faculty of Science, Palacký University Olomouc, 78371 Olomouc, Czech Republic; Department of Materials Science and Engineering, University of Erlangen-Nuremberg, D-91058 Erlangen, Germany;* orcid.org/0000-0002-9208-5771

Complete contact information is available at:
https://pubs.acs.org/10.1021/acs.nanolett.0c00594

■ REFERENCES

(1) International Energy Agency (IEA, Paris). www.iea.org. www.iea.org/reports/renewables (accessed October 29, 2019). Market Report Series: Renewables 2018 Analysis and Forecasts to 2023.

(2) International Renewable Energy Agency (IRENA). Concentrating Solar Power. *Renewable Energy Technologies*; Cost Analysis Series, Vol. *1*: Power Sector, 2012.

(3) Maier, S. A.; Brongersma, M. L.; Kik, P. G.; Meltzer, S.; Requicha, A. A. G.; Atwater, H. A. Plasmonics—A Route to Nanoscale Optical Devices. *Adv. Mater.* **2001**, *13*, 1501−1505.

(4) Christopher, P.; Xin, H.; Linic, S. Visible-light-enhanced Catalytic Oxidation Reactions on Plasmonic Silver Nanostructures. *Nat. Chem.* **2011**, *3*, 467−472.

(5) Swearer, D. F.; Zhao, H.; Zhou, L.; Zhang, C.; Robatjazi, H.; Martinez, J. M. P.; Krauter, C. M.; Yazdi, S.; McClain, M. J.; Ringe, E.; Carter, E. A.; Nordlander, P.; Halas, N. J. Heterometallic Antenna−reactor Complexes for Photocatalysis. *Proc. Natl. Acad. Sci. U. S. A.* **2016**, *113*, 8916−8920.

(6) Brongersma, M. L.; Shalaev, V. M. The Case for Plasmonics. *Science* **2010**, *328*, 440−441.

(7) Haffner, C.; Chelladurai, D.; Fedoryshyn, Y.; Josten, A.; Baeuerle, B.; Heni, W.; Watanabe, T.; Cui, T.; Cheng, B.; Saha, S.; Elder, D. L.; Dalton, L. R.; Boltasseva, A.; Shalaev, V. M.; Kinsey, N.; Leuthold, J. Low-loss Plasmon-assisted Electro-optic Modulator. *Nature* **2018**, *556*, 483−486.

(8) Baffou, G.; Quidant, R. Thermo-plasmonics: Using Metallic Nanostructures as Nano-sources of Heat. *Laser Photonics Rev.* **2013**, *7*, 171−187.

(9) Govorov, A. O.; Zhang, W.; Skeini, T.; Richardson, H.; Lee, J.; Kotov, N. A. Gold Nanoparticle Ensembles as Heaters and Actuators: Melting and Collective Plasmon Resonances. *Nanoscale Res. Lett.* **2006**, *1*, 84.

(10) Lal, S.; Clare, S. E.; Halas, N. J. Nanoshell-Enabled Photothermal Cancer Therapy: Impending Clinical Impact. *Acc. Chem. Res.* **2008**, *41*, 1842−1851.

(11) Hirsch, L. R.; Stafford, R. J.; Bankson, J. A.; Sershen, S. R.; Rivera, B.; Price, R. E.; Hazle, J. D.; Halas, N. J.; West, J. L. Nanoshell-mediated Near-infrared Thermal Therapy of Tumors Under Magnetic Resonance Guidance. *Proc. Natl. Acad. Sci. U. S. A.* **2003**, *100*, 13549−13554.

(12) Adleman, J. R.; Boyd, D. A.; Goodwin, D. G.; Psaltis, D. Heterogenous Catalysis Mediated by Plasmon Heating. *Nano Lett.* **2009**, *9*, 4417−4423.

(13) Neumann, O.; Urban, A. S.; Day, J.; Lal, S.; Nordlander, P.; Halas, N. J. Solar Vapor Generation Enabled by Nanoparticles. *ACS Nano* **2013**, *7*, 42−49.

(14) Zhou, L.; Tan, Y.; Wang, J.; Xu, W.; Yuan, Y.; Cai, W.; Zhu, S.; Zhu, J. 3D Self-assembly of Aluminium Nanoparticles for Plasmon-enhanced Solar Desalination. *Nat. Photonics* **2016**, *10*, 393−398.

(15) Boyd, D. A.; Greengard, L.; Brongersma, M.; El-Naggar, M. Y.; Goodwin, D. G. Plasmon-Assisted Chemical Vapor Deposition. *Nano Lett.* **2006**, *6*, 2592−2597.

(16) Cao, L.; Barsic, D. N.; Guichard, A. R.; Brongersma, M. L. Plasmon-Assisted Local Temperature Control to Pattern Individual Semiconductor Nanowires and Carbon Nanotubes. *Nano Lett.* **2007**, *7*, 3523−3527.

(17) Righini, M.; Zelenina, A. S.; Girard, C.; Quidant, R. Parallel and Selective Trapping in a Patterned Plasmonic Landscape. *Nat. Phys.* **2007**, *3*, 477−480.

(18) Ndukaife, J. C.; Kildishev, A. V.; Nnanna, A. G. A.; Shalaev, V. M.; Wereley, S. T.; Boltasseva, A. Long-range and Rapid Transport of Individual Nano-objects by a Hybrid Electrothermoplasmonic Nanotweezer. *Nat. Nanotechnol.* **2016**, *11*, 53−59.

(19) Berthelot, J.; Aćimović, S. S.; Juan, M. L.; Kreuzer, M. P.; Renger, J.; Quidant, R. Three-dimensional Manipulation with Scanning Near-field Optical Nanotweezers. *Nat. Nanotechnol.* **2014**, *9*, 295−299.

(20) Grigorenko, A. N.; Roberts, N. W.; Dickinson, M. R.; Zhang, Y. Nanometric Optical Tweezers Based on Nanostructured Substrates. *Nat. Photonics* **2008**, *2*, 365−370.

(21) Challener, W. A.; Peng, C.; Itagi, A. V.; Karns, D.; Peng, W.; Peng, Y.; Yang, X.; Zhu, X.; Gokemeijer, N. J.; Hsia, Y.-T.; Ju, G.; Rottmayer, R. E.; Seigler, M. A.; Gage, E. C. Heat-assisted Magnetic Recording by a Near-field Transducer with Efficient Optical Energy Transfer. *Nat. Photonics* **2009**, *3*, 220−224.

(22) Zhou, N.; Xu, X.; Hammack, A. T.; Stipe, B. C.; Gao, K.; Scholz, W.; Gage, E. C. Plasmonic Near-field Transducer for Heat-assisted Magnetic Recording. *Nanophotonics* **2014**, *3*, 141−155.

(23) Guler, U.; Kildishev, A. V.; Boltasseva, A.; Shalaev, V. M. Plasmonics on the Slope of Enlightenment: the Role of Transition Metal Nitrides. *Faraday Discuss.* **2015**, *178*, 71−86.

(24) Mutlu, M.; Kang, J.-H.; Raza, S.; Schoen, D.; Zheng, X.; Kik, P. G.; Brongersma, M. L. Thermoplasmonic Ignition of Metal Nanoparticles. *Nano Lett.* **2018**, *18*, 1699−1706.

(25) Chou, J. B.; Yeng, Y. X.; Lee, Y. E.; Lenert, A.; Rinnerbauer, V.; Celanovic, I.; Soljačić, M.; Fang, N. X.; Wang, E. N.; Kim, S.-G. Enabling Ideal Selective Solar Absorption with 2D Metallic Dielectric Photonic Crystals. *Adv. Mater.* **2014**, *26*, 8041−8045.

(26) Rinnerbauer, V.; Lenert, A.; Bierman, D. M.; Yeng, Y. X.; Chan, W. R.; Geil, R. D.; Senkevich, J. J.; Joannopoulos, J. D.; Wang, E. N.; Soljačić, M.; Celanovic, I. Metallic Photonic Crystal Absorber-Emitter for Efficient Spectral Control in High-Temperature Solar Thermophotovoltaics. *Adv. Energy Mater.* **2014**, *4*, 1400334.

(27) Arpin, K. A.; Losego, M. D.; Cloud, A. N.; Ning, H.; Mallek, J.; Sergeant, N. P.; Zhu, L.; Yu, Z.; Kalanyan, B.; Parsons, G. N.; Girolami, G. S.; Abelson, J. R.; Fan, S.; Braun, P. V. Three-dimensional Self-assembled Photonic Crystals with High Temperature Stability for Thermal Emission Modification. *Nat. Commun.* **2013**, *4*, 2630.

(28) Guler, U.; Boltasseva, A.; Shalaev, V. M. Refractory Plasmonics. *Science* **2014**, *344*, 263−264.

(29) Ishii, S.; Sugavaneshwar, R. P.; Nagao, T. Titanium Nitride Nanoparticles as Plasmonic Solar Heat Transducers. *J. Phys. Chem. C* **2016**, *120*, 2343−2348.

(30) Gui, L.; Bagheri, S.; Strohfeldt, N.; Hentschel, M.; Zgrabik, C. M.; Metzger, B.; Linnenbank, H.; Hu, E. L.; Giessen, H. Nonlinear Refractory Plasmonics with Titanium Nitride Nanoantennas. *Nano Lett.* **2016**, *16*, 5708−5713.

(31) Briggs, J. A.; Naik, G. V.; Zhao, Y.; Petach, T. A.; Sahasrabuddhe, K.; Goldhaber-Gordon, D.; Melosh, N. A.; Dionne, J. A. Temperature-dependent Optical Properties of Titanium Nitride. *Appl. Phys. Lett.* **2017**, *110*, 101901.

(32) Naik, G. V.; Shalaev, V. M.; Boltasseva, A. Alternative Plasmonic Materials: Beyond Gold and Silver. *Adv. Mater.* **2013**, *25*, 3264−3294.

(33) Braic, L.; Vasilantonakis, N.; Mihai, A.; Villar Garcia, I. J.; Fearn, S.; Zou, B.; Alford, N. M.; Doiron, B.; Oulton, R. F.; Maier, S. A.; Zayats, A. V.; Petrov, P. K. Titanium Oxynitride Thin Films with Tunable Double Epsilon-Near-Zero Behavior for Nanophotonic Applications. *ACS Appl. Mater. Interfaces* **2017**, *9*, 29857−29862.

(34) Naldoni, A.; Guler, U.; Wang, Z.; Marelli, M.; Malara, F.; Meng, X.; Besteiro, L. V.; Govorov, A. O.; Kildishev, A. V.; Boltasseva, A.; Shalaev, V. M. Broadband Hot-Electron Collection for Solar Water Splitting with Plasmonic Titanium Nitride. *Adv. Opt. Mater.* **2017**, *5*, 1601031.

(35) Li, W.; Guler, U.; Kinsey, N.; Naik, G. V.; Boltasseva, A.; Guan, J.; Shalaev, V. M.; Kildishev, A. V. Refractory Plasmonics with Titanium Nitride: Broadband Metamaterial Absorber. *Adv. Mater.* **2014**, *26*, 7959−7965.

(36) Reddy, H.; Guler, U.; Kildishev, A. V.; Boltasseva, A.; Shalaev, V. M. Temperature-dependent Optical Properties of Gold Thin Films. *Opt. Mater. Express* **2016**, *6*, 2776−2802.

(37) Reddy, H.; Guler, U.; Chaudhuri, K.; Dutta, A.; Kildishev, A. V.; Shalaev, V. M.; Boltasseva, A. Temperature-Dependent Optical Properties of Single Crystalline and Polycrystalline Silver Thin Films. *ACS Photonics* **2017**, *4*, 1083−1091.

(38) Reddy, H.; Guler, U.; Kudyshev, Z.; Kildishev, A. V.; Shalaev, V. M.; Boltasseva, A. Temperature-Dependent Optical Properties of Plasmonic Titanium Nitride Thin Films. *ACS Photonics* **2017**, *4*, 1413−1420.

(39) Riboni, F.; Nguyen, N. T.; So, S.; Schmuki, P. Aligned Metal Oxide Nanotube Arrays: Key-aspects of Anodic TiO_2 Nanotube Formation and Properties. *Nanoscale Horiz* **2016**, *1*, 445−466.

(40) Guler, U.; Shalaev, V. M.; Boltasseva, A. Nanoparticle Plasmonics: Going Practical with Transition Metal Nitrides. *Mater. Today* **2015**, *18*, 227−237.

(41) Mayadas, A. F.; Shatzkes, M. Electrical-Resistivity Model for Polycrystalline Films: the Case of Arbitrary Reflection at External Surfaces. *Phys. Rev. B* **1970**, *1*, 1382−1389.

(42) Mayadas, A. F.; Shatzkes, M.; Janak, J. F. Electrical Resistivity Model for Polycrystalline Films: The Case of Specular Reflection at External Surfaces. *Appl. Phys. Lett.* **1969**, *14*, 345−347.

(43) Celanovic, I.; Jovanovic, N.; Kassakian, J. Two-dimensional Tungsten Photonic Crystals as Selective Thermal Emitters. *Appl. Phys. Lett.* **2008**, *92*, 193101.

(44) Chen, K.-P.; Drachev, V. P.; Borneman, J. D.; Kildishev, A. V.; Shalaev, V. M. Drude Relaxation Rate in Grained Gold Nanoantennas. *Nano Lett.* **2010**, *10*, 916−922.

(45) Chawla, J. S.; Zhang, X. Y.; Gall, D. Effective Electron Mean Free Path in TiN(001). *J. Appl. Phys.* **2013**, *113*, 063704.

(46) Johnson, P. B.; Christy, R. W. Optical Constants of the Noble Metals. *Phys. Rev. B* **1972**, *6*, 4370−4379.

(47) Olmon, R. L.; Slovick, B.; Johnson, T. W.; Shelton, D.; Oh, S.-H.; Boreman, G. D.; Raschke, M. B. Optical Dielectric Function of Gold. *Phys. Rev. B: Condens. Matter Mater. Phys.* **2012**, *86*, 235147.

(48) Yang, H. U.; D'Archangel, J.; Sundheimer, M. L.; Tucker, E.; Boreman, G. D.; Raschke, M. B. Optical Dielectric Function of Silver. *Phys. Rev. B: Condens. Matter Mater. Phys.* **2015**, *91*, 235137.

(49) Chawla, J. S.; Gstrein, F.; O'Brien, K. P.; Clarke, J. S.; Gall, D. Electron Scattering at Surfaces and Grain Boundaries in Cu Thin Films and Wires. *Phys. Rev. B: Condens. Matter Mater. Phys.* **2011**, *84*, 235423.

(50) Piallat, F.; Gassilloud, R.; Caubet, P.; Vallee, C. Investigation of TiN Thin Film Oxidation Depending on the Substrate Temperature at Vacuum Break. *J. Vac. Sci. Technol., A* **2016**, *34*, 051508.